
Article:
Rankine, Conor D, Nunes, João Pedro F, Feixas, Tomas W B Lock et al. (2 more authors) (2018) Structure of 4-(Dimethylamino)benzonitrile Using Gas Electron Diffraction : A New Lease of Life for the Only Gas Electron Diffractometer in the UK. Journal of Physical Chemistry A. pp. 5656-5665. ISSN 1089-5639

https://doi.org/10.1021/acs.jpca.8b03613

The Structure of 4-(Dimethylamino)benzonitrile Using Gas Electron Diffraction: A New Lease of Life for the Only Gas Electron Diffractometer in the UK

Conor D. Rankine[‡]*, João Pedro F. Nunes*[‡]*, Tomas Lock Feixas, Stuart Young and Derek A. Wann*[‡,]*

Department of Chemistry, University of York, Heslington, York, U.K, YO10 5DD

ABSTRACT

The continued demand for gas-phase structures has led to the recommissioning of a gas electron diffractometer, formerly housed at the University of Reading. The gas electron diffractometer, now the only one of its kind in the UK, is currently housed at the University of York where it is now used routinely to determine directly structures of isolated molecules in the gas phase. The instrument has been outfitted with an air-heated nozzle assembly to increase the range of molecules accessible to study in the gas phase; the efficacy of this assembly is demonstrated in this article *via* the direct determination of the gas-phase structure of 4-(dimethylamino)benzonitrile (DMABN) at high temperature. A series of complementary

theoretical calculations using the B2PLYP DFT functional of Grimme *et al.* with correlation-consistent basis sets of double, triple and quadruple-ζ quality are also presented. The agreement between the experimental and theoretical structural parameters attests to the accuracy of the applied theoretical calculations and of our gas-phase structural solution.

INTRODUCTION.

The recent renaissance of the gas electron diffraction (GED) technique has been driven by the prospect of recording ever-better gas-phase "molecular movies" in pioneering ultrafast electron diffraction (UED)[1-4] experiments. GED instruments are not commercially available today and all those that are currently in existence[5-9] have been built (or heavily modified from discontinued commercial models) in-house over many years by generations of researchers. This is true of our own GED instrument, a description of which is provided in this article. We demonstrate the usefulness of the instrument and affirm the relevance of the GED technique *via* the direct determination of the gas-phase structure of 4-(dimethylamino)benzonitrile (DMABN).

The University of York GED instrument was formerly housed at the University of Reading and was initially commissioned in the late 1960s. During the 1990s and into the first decade of the new millennium, Aarset, Rice and Page oversaw a particularly prolific period of operation[10-15] in which many gas-phase structures of organometallics and small organic and main-group molecules were characterized using the instrument, and collaborative work was carried out with other electron diffractionists including Rankin[16] and Hedberg.[17] The instrument was acquired by the University of York in 2015 and this article details the recommissioning of the instrument and describes the contemporary GED experiment. The instrument has been fitted with an air-heated

sample delivery system which allows low-volatility compounds to be made accessible to study *via* GED; DMABN as reported here is such an example.

DMABN is the archetypal example of the photophysical phenomenon of dual fluorescence, first characterized by Lippert *et al.* in 1961.[18] Not only does DMABN fluoresce with two different wavelengths (the fluorescence spectrum containing one 'normal' band that is slightly Stokes-shifted and one 'anomalous' band that is heavily red-shifted), the fluorescence spectrum is heavily dependent on experimental conditions such as solvent polarity (when in solution) and temperature. There are scarcely any comparable examples in the chemical literature of such an apparently simple organic molecule fueling such intense research activity,[19-50] both experimental[19-26,29,32,34,35,41] and theoretical,[27,28,30,31,33,36-40,47-50] from which no concrete conclusions have yet been drawn. In an attempt to rationalize experimental observations, advanced theoretical methods have been put to the test on DMABN over the last decade {MCSCF/MRPT2,[27,28] MR-CISD,[47] EOM-CCSD,[30] ADC(2),[47,48] LR-TDDFT,[49,50] among others} and examples exist in the literature in which these theoretical methods have been coupled with surface-hopping molecular dynamics (SHMD) simulations.[48-50] The natural application of these theoretical methods is to the gas-phase – rather than the solution-phase – photophysics of DMABN. To the best of our knowledge, no complete and directly-obtained gas-phase structural solution has yet been reported for DMABN in the ground electronic state, yet this is surely the starting point for direct gas-phase structural studies of DMABN in the relevant electronically-excited states *via* UED. We are aware only of the partial gas-phase structural solutions of Kajimoto *et al.*[51] and Pratt *et al.*,[52] obtained *via* microwave spectroscopy (MWS), and the solid-state X-ray diffraction (XRD) solutions of Heine *et al.*[53] for DMABN and a range of analogous aminobenzonitriles. As demonstrated by Mitzel *et al.*[54-58] in a number of publications, the

differences between molecular structures in the gas phase and in the solid state are non-negligible and are, in certain cases, notably larger than the accuracy of the theoretical methods that are readily available today.

One of the most valuable prerequisites to a UED experiment is a pre-time-zero (ground-state) experimental gas-phase structural solution obtained via GED; we present such a solution here.

GAS ELECTRON DIFFRACTOMETER.

The University of York GED instrument, photographed in Figure 1 and schematically illustrated in Figure 2, comprises three modules: the column, the chamber, and the detector, housing the electron source, sample delivery system and electron detection system, respectively. An electron beam shutter acts as a gate valve, delimiting the column module and the chamber and detector modules; the latter two modules are not delimited.

Vacuum System. The delimitation of the column module and chamber module allows for differential pumping of the instrument. The column module and chamber module can be reduced to pressures in the range of 10^{-5} to 10^{-6} mbar using two dedicated oil diffusion pumps (Edwards E06 and E04, respectively) backed by a belt-drive rotatory pump (Edwards ED200). Remotely-operated pneumatic butterfly valves (Edwards QSB5P and Edwards QSB3P) and solenoid valves (Edwards PLV25P) regulate the pumping of the apparatus.

Figure 1. Photograph of the University of York GED instrument described in this article taken during routine operation.

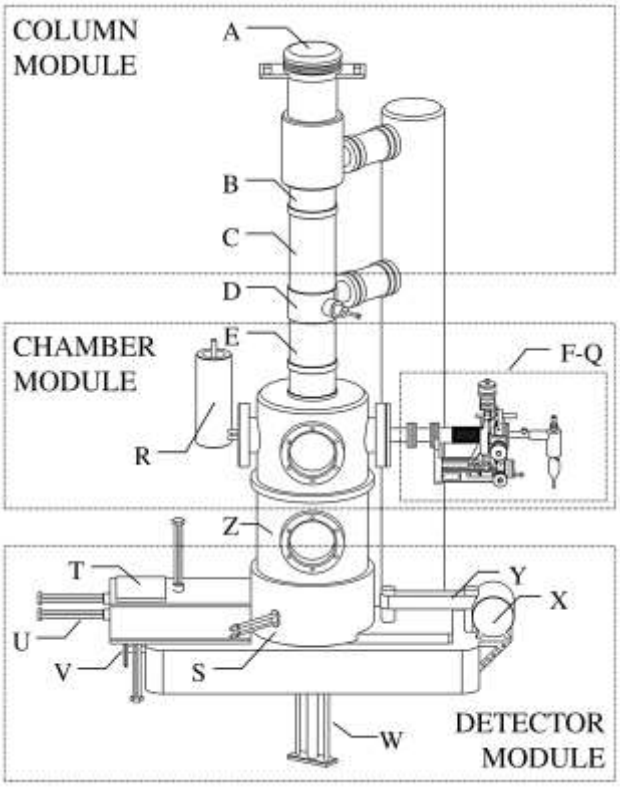

Figure 2. Schematic illustration of the University of York GED instrument described in this article. The electron source (**A**), solenoid deflectors (**B**), electron flight tube (**C**), electron beam shutter (**D**), solenoid lens (**E**), air-heated nozzle assembly (**F-Q**), liquid nitrogen trap (**R**), retractable scintillator screen (**S**), image plate magazine (**T**), image plate manipulator levers (**U**) and crank (**V**), image plate lift/pneumatic actuator (**W**), rotating sector drive motor (**X**) and belt (**Y**) and spacer module (**Z**) are indicated. Components **A**-**Z** are described in the main text. Components associated with the vacuum system described in the main text are omitted from the schematic for clarity.

Electron Source and Optics. The electron source (**A**), mounted at the top of the column module, comprises a tungsten hairpin filament (Agar A050), photographed in Figure 3a, tantalum Wehnelt cap, and stainless steel anode plug arranged in the classic 'triode'[59] electron gun geometry. A high-voltage power supply (Start Spellman) is used to provide a variable accelerating potential (typically set to 42.2 kV) to produce an electron beam with defined electron emission current and electron wavelength (approximately 0.66 μA and 6.0 pm,

respectively, at 42.2 kV). Two sets of solenoid deflectors (**B**), photographed in Figure 3b, guide the electron beam through a flight tube (**C**) and platinum collimating aperture mounted inside the electron beam shutter (**D**). The electron beam shutter is photographed in Figure 3c. The transverse profile and focal length of the electron beam is controlled *via* a solenoid lens (**E**).

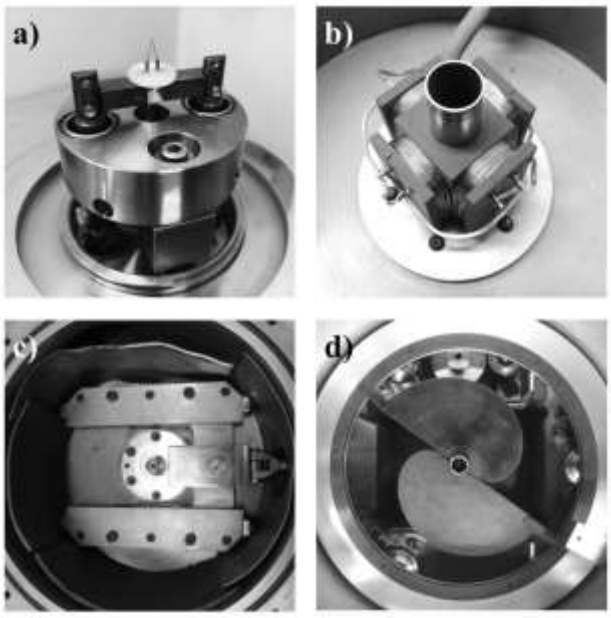

Figure 3. Photographs of a) the tungsten hairpin filament and mount, b) the sets of solenoid deflectors, c) the electron beam shutter, and d) the rotating sector.

Sample Delivery System. An air-heated nozzle, schematically illustrated in Figure 4, has been machined to allow samples with low volatility at room temperature to be delivered into the chamber module at the point of diffraction. The air-heated nozzle is coupled to a triple-axis flange-mounted translator (**F**) and positioned such that the nozzle tip is approximately 250 – 500 μm from the axis of propagation of the electron beam. A continuous flow of pressurized air (50 psi) is heated using in-line cartridge heaters and branched before circulation around the nozzle shaft (**G**) and sample ampoule (**H**) *via* two air flow routes with independent air inlets (**I**, **J**) and

outlets (**K**, **L**). Two independent proportional-integral-derivative (PID) controllers regulate the power delivered to the in-line cartridge heaters, providing reliable temperature stability of ±1 °C. A temperature gradient of at least 5 °C is typically maintained between the nozzle tip (**M**) and the sample ampoule, preventing the sample from condensing inside the delivery line (**N**) and blocking the flow of sample into the chamber module. The sample ampoule and the delivery line are delimited by a needle valve (**O**), which allows for fine control of the gaseous sample intake. Two clean-up apertures secured onto the nozzle shaft ensure the optimum beam quality is achieved at the point of diffraction. The first clean-up aperture (**P**), 15 mm in diameter, is positioned a few centimeters above the point of diffraction and precludes stray electrons travelling at large angles from reaching and saturating the detector. The second clean-up aperture (**Q**), 1 mm in diameter, is positioned a few millimeters above the point of diffraction and helps to collimate the beam before interaction with the gaseous sample. A liquid nitrogen trap (**R**) is mounted opposite the air-heated nozzle assembly. The liquid nitrogen trap condenses the gaseous sample after interaction with the electron beam, thereby preventing secondary scattering events and reducing the background signal.

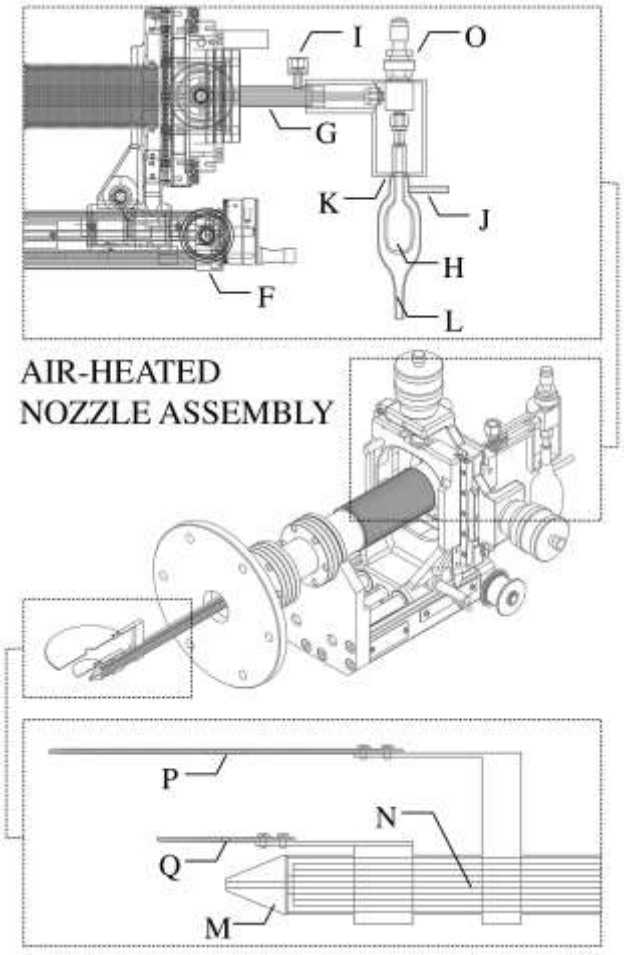

Figure 4. Schematic illustration of the air-heated nozzle. The nozzle shaft and apertures are cut away; expanded cross-section views of the nozzle tip and the sample reservoir are presented. The triple-axis flange-mounted translator (**F**), nozzle shaft (**G**), sample ampoule (**H**), air inlets (**I**, **J**), air outlets (**K**, **L**), nozzle tip (**M**), sample delivery line (**N**), needle valve (**O**), 15 mm clean-up aperture (**P**) and 1 mm clean-up aperture (**Q**) are indicated. Components **F**-**Q** are described in the main text.

Electron Detection System. Before data acquisition, it is possible to visually inspect the brightness and shape of the electron beam using a retractable scintillator screen (**S**). During data acquisition, diffraction on interaction of the electron beam with the gaseous sample is recorded on reusable image plates (Fuji BAS-IP MS 2025); these image plates comprise thin polyester films coated with barium fluorobromide grains doped with trace amounts of europium. An

individual image plate can be reused thousands of times, on the condition that they are not exposed to intense radiation and are kept clean and contaminant-free. The image plate magazine (**T**) can contain up to five image plates mounted onto aluminum holders which are cycled into (before exposure) and out of (after exposure) the detector module manually *via* actuation of four levers (**U**) that translate the mounted image plates within the image plate magazine and a crank (**V**) that drives a conveyor belt used to translate the mounted image plates from the image plate magazine and into position above a pneumatic actuator (**W**). The pneumatic actuator is located below the detector module and lifts and lowers the plates to and from their data acquisition position below the rotating sector, photographed in Figure 3d. The rotating sector compensates for the steep drop-off in diffraction intensity as a function of scattering angle by shading the inner portion of the image plate to a greater extent than the outer portion. Rotation of the rotating sector effectively applies an r^3-type function to the acquired data, where r is the distance from the center of the diffraction data; the dynamic range of the detector is improved considerably. An external AC motor (**X**) and belt (**Y**) drives the rotating sector at ≈ 144 rpm. The entire detector module is mounted on long-travel linear translator (omitted from Figure 2 for clarity) which allows for data acquisition at two different nozzle-to-image-plate distances. For data acquisition at the longer of the two possible nozzle-to-image-plate distances, a spacer module (**Z**) is added to close the gap between the chamber and the detector; for data acquisitions at the shorter of the two possible nozzle-to-image-plate distances, it is removed.

EXPERIMENTAL METHODOLOGY.

DMABN was purchased from Sigma-Aldrich (ALDRICH-D139505, 4-(dimethylamino)benzonitrile, 98%) and used without subsequent purification. GED data for DMABN were acquired using the University of York GED instrument detailed in the previous section of this article. An accelerating potential of 42.22 keV was applied to produce an electron emission current of 0.66 μA and an electron wavelength of approximately 6.0 pm. The scattered electrons were recorded *via* exposures of image plates (Fuji BAS-IP MS 2025) at nozzle-to-image-plate distances of 234.5 and 487.0 mm. Three exposures were recorded at each nozzle-to-image-plate distance. The sample of DMABN and the nozzle were heated to 371 and 393 K, respectively, during exposures at the longer nozzle-to-image-plate distance and to 395 and 413 K, respectively, during exposures at the shorter nozzle-to-image-plate distance. A flatbed image plate scanner (Fuji BAS-1800II) was used to digitize the scattering intensities recorded on the image plates. A summary of the experimental conditions is found in Table S1.

THEORETICAL METHODOLOGY.

The ground-state structure of DMABN and atomic labelling scheme referred to throughout this article is outlined in Figure 5.

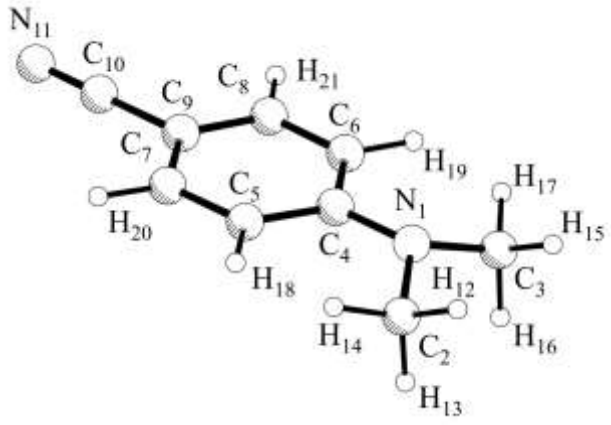

Figure 5. The ground-state structure of DMABN; the atomic labelling scheme is outlined.

All theoretical calculations were carried out using the Gaussian09 Rev. D01[60] software suite. The highest-level geometry optimizations of DMABN were carried out in the C_s symmetry point group using the double-hybrid B2PLYP[61] density functional of Grimme and a range of basis sets (cc-pVDZ, cc-pVTZ and cc-pVQZ)[62] of increasing completeness. Optimized bonded internuclear distances were extrapolated to the complete basis set (CBS) limit to give theoretical results denoted B2PLYP/CBS *via* fitting of the bonded internuclear distances, r_{ij}, determined at the B2PLYP/cc-pVDZ, B2PLYP/cc-pVTZ and B2PLYP/cc-pVQZ levels with a function of the form:

$$r_{ij}(x) = r_{ij,CBS} + \beta e^{-\alpha x}, x \in \{2,3,4\}$$

in which $r_{ij,CBS}$ is the internuclear distance r_{ij} at the CBS limit and α and β are fitting parameters. To establish flexible restraints for use in a SARACEN-type[63-65] GED refinement, additional geometry optimizations were carried out in the C_s symmetry point group using the B3LYP,[66,67] B3P86,[66,68] B3PW91,[66,69] PBEH1PBE[70] and HSEH1PBE[71-74] density functionals and the cc-pVDZ, cc-pVTZ and cc-pVQZ basis sets. Optimized bonded internuclear distances were

similarly fitted with the function outlined in Eq.1 to give CBS limit theoretical results. The characters of all optimized geometries were verified using vibrational frequency analysis and all were confirmed to correspond to minima on the ground-state potential energy surface. Cartesian coordinates of all optimized geometries are found in Tables S2-19.

Theoretical r_{h1}-type amplitudes of vibration (u_{h1}) and curvilinear distance corrections (k_{h1}) were generated from a harmonic force field computed at the B2PLYP/cc-pVDZ level using the SHRINK[75,76] software package.

REDUCTION AND REFINEMENT.

Digitized diffraction patterns were reduced to molecular intensity curves (MICs) using an azimuthal averaging routine implemented in the in-house-developed data extraction package, *xtract*.[77] MICs were refined using the ed@ed v3.0[78] least-squares refinement package, employing the electron scattering factors of Ross *et al.*[79] The weighting points for off-diagonal weight matrices, scaling factors, and correlation parameters can be found in Table S20. The correlation matrix can be found in Table S21. The least-squares refinement procedure used the SARACEN[63-65] approach and yielded internuclear distances of the r_{h1} type; r_{h1}-type internuclear distances are related to the vibrationally-averaged r_a-type distances determined directly *via* the GED experiment by the relationship $r_{h1} \approx r_a + u_{h1}^2/r_a - k_{h1}$.

The least-squares refinement procedure employed a parameterized molecular model describing DMABN in terms of 16 refinable parameters comprising nine distances ($p_1 - p_9$), five angles ($p_{10} - p_{14}$) and two dihedral angles (p_{15} and p_{16}). Using simplifications that were predicted by all theoretical results, the C_s symmetry of DMABN, planarity of the benzonitrile subunit, and linearity of the nitrile subunit were exploited in order to construct the parameterized molecular

model such that it required as few refinable parameters as possible. A full description of this parameterized molecular model (comprising Eq.S1-32) is found in the supplementary information associated with this article. With the exception of the C≡N bond ($r_{10,11}$; 116.0 pm, B2PLYP/CBS), our highest-level B2PLYP/CBS theoretical results indicated that all other internuclear distances between heavy nuclei in DMABN ($r_{1,2}$, $r_{1,4}$, $r_{4,5}$, $r_{5,7}$, $r_{7,9}$ and $r_{9,10}$) were similar, being associated with a reasonably narrow range (7.7 pm) and small standard deviation (2.6 pm). The correlation of these six internuclear distances could be expected to prove an obstacle to an independent structural refinement; consequently, p_1 was defined within the parameterized molecular model as a multiplicity-weighted average of these internuclear distances (Eq.S1) and p_2 to p_6 as refinable difference parameters (Eq.S2-6). These six internuclear distances were then represented within the parameterized molecular model as linear combinations of p_1 to p_6 (Eq.S7-12).

Six additional non-refinable parameters, f_1 to f_6, describing differences in internuclear distance of ≤ 0.5 pm and in angles and dihedrals of ≤ 2.0° were incorporated into the model only for structural parameters containing a combination of heavy nuclei and light nuclei in their description.

SARACEN[63-65] restraints were based on the values obtained in our highest-level B2PLYP/CBS theoretical data and applied to 11 of the 16 refinable parameters with the remaining five being allowed to refine free from restraint. Estimates of the uncertainties associated with the SARACEN[63-65] restraint values were derived from sequential DFT geometry optimizations using the B2PLYP, B3LYP, B3P86, B3PW91, PBEH1PBE and HSEH1PBE functionals with the cc-pVDZ, cc-pVTZ and cc-pVQZ basis sets.

A full summary of the refined (r_{h1}-type) and theoretical (r_e-type, B2PLYP/CBS) parameters p_1 to p_{16} accompanied by uncertainties can be found in Table S22. The values of non-refinable parameters f_1 to f_6 were established at the B2PLYP/CBS level and are tabulated in Table S23.

All amplitudes of vibration associated with a given peak in the radial distribution curve (RDC) were tied using a fixed ratio to the amplitude of vibration associated with the nuclear pair that gave rise to the largest scattering effect under that peak. Only this amplitude of vibration was refined for each peak in the RDC. All internuclear distances, refined and theoretical amplitudes of vibration, r_{h1}-type distance corrections, and SARACEN[63-65] restraints (where applied) are tabulated in Table S24.

RESULTS.

The experimentally-acquired and experimental-minus-theoretical 'difference' MICs are presented in Figure 6. Fourier transformation of the MIC yields the radial distribution curve (RDC); experimentally-acquired and experimental-minus-theoretical 'difference' RDCs are presented in Figure 7.

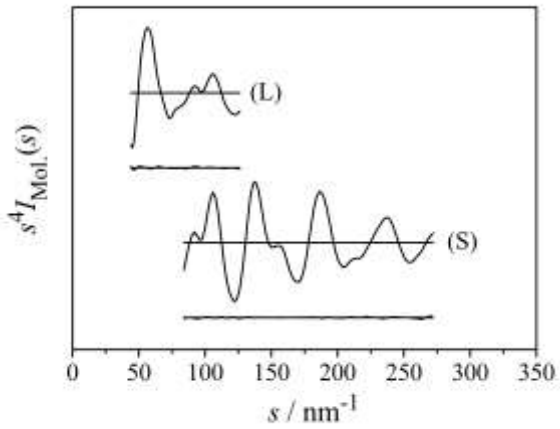

Figure 6. MICs and experimental-minus-theoretical 'difference' MICs acquired on reduction of a) long and b) short GED data collected for DMABN.

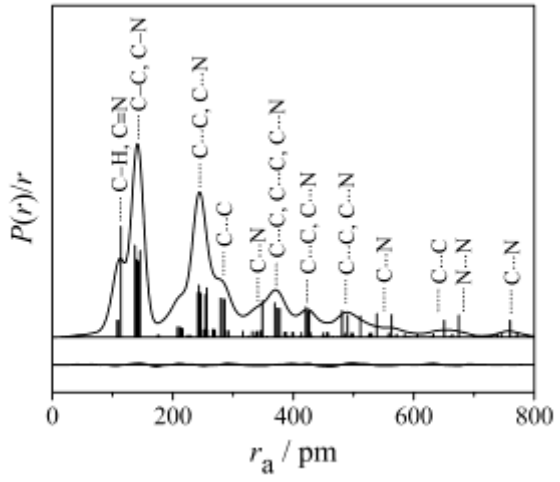

Figure 7. RDC and experimental-minus-theoretical 'difference' RDC acquired on refinement of GED data collected for DMABN.

The R_G factor obtained for the least-squares refinement of **A** was 0.055; the R_D factor (which ignores the off-diagonal elements of the weight matrix) was 0.036. For the reader unfamiliar with the difference between the R_G and R_D factors, Ref. 80 is instructive. Refined Cartesian coordinates for the r_{h1}-type GED structure of DMABN can be found in Table S25.

A visual overview of the refined experimental internuclear distances and angles is given in Figure 8 alongside values for the same structural parameters obtained in our highest-level B2PLYP/CBS theoretical calculations.

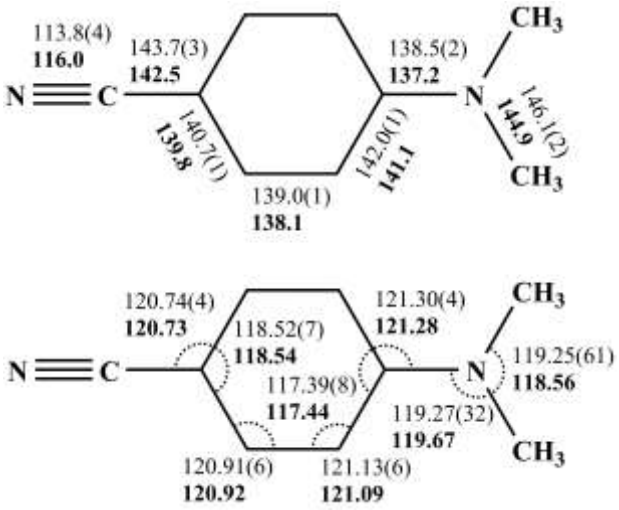

Figure 8. Experimental r_{h1}-type GED (regular text) and theoretical B2LPYP/CBS (bold text) geometric parameters determined for DMABN. All internuclear distances (upper diagram) are reported in picometers; all angles (lower diagram) are reported in degrees.

DISCUSSION.

Uncertainties are low for all structural parameters, with internuclear distances and angles typically being determined to within a few tenths of a picometer and a few tenths of a degree, respectively. All internuclear distances and angles between nuclei are well-determined by GED to 0.8(3) pm and 0.1(2)° of their theoretical values at this level, attesting to the high accuracy of the B2PLYP functional of Grimme for this application.

In Table 1, refined experimental internuclear distances and angles are tabulated alongside our B2PLYP/CBS theoretical calculations and data reported for crystalline and gas-phase DMABN

in earlier X-ray diffraction (Heine *et al.*)[53] and microwave spectroscopy (Kajimoto *et al.*)[51] experiments, respectively.

Our structural solution exhibits qualitatively acceptable agreement with the XRD solution; all internuclear distances between heavy nuclei are determined to 1.5(6) pm of their XRD values and their ratios to one another (which may be qualitatively predicted in a straightforward manner *via* valence bond theory) are well-conserved.

We note the minor systematic deviation towards shorter internuclear distances in the XRD solution; all internuclear distances between heavy nuclei (with the exception of the C≡N bond, $r_{10,11}$) are shorter by a factor of 0.988(1). This deviation is documented[81] and might be expected where comparisons are made between internuclear distances derived from r_{h1}-type approximate equilibrium structures and from thermally-averaged reciprocal lattice positions determined in GED and XRD experiments, respectively. It is difficult to comment on the extent to which our gas-phase structure agrees with the MWS solution as only three structural parameters ($r_{1,4}$, $r_{9,10}$ and $a_{2,1,3}$) were reported without accompanying uncertainties.

Our comments on the three key structural subunits of DMABN – the nitrile, benzyl and dimethylamino – follow.

Table 1. Summary of refined (r_{h1}) GED, theoretical (r_e, B2PLYP/CBS), XRD[53] (recorded at 253 K) and microwave spectroscopic[51] measurements of internuclear distances[a] and angles[b] in DMABN.

Structural Parameter	GED (r_{h1})	r_e	XRD[53]	MWS[51]
$r_{1,2}$	146.1(2)	144.9	144.9(3)[c]	–
$r_{1,4}$	138.5(2)	137.2	136.5(3)	137.9[e]
$r_{4,5}$	142.0(1)	141.1	140.0(4)	–
$r_{5,7}$	139.0(1)	138.1	137.0(4)	–
$r_{7,9}$	140.7(1)	139.8	138.8(4)	–
$r_{9,10}$	143.7(3)	142.5	142.7(5)	145.4[e]
$r_{10,11}$	113.8(3)	116.0	114.5(4)	–
$r_{2,12}$	108.7(4)	108.4	96.0[f]	–
$r_{2,13}$	109.6(4)	109.3	96.0[f]	–
$r_{2,14}$	109.2(4)	108.9	96.0[f]	–
$r_{5,18}$	107.7(4)	107.7	93.0[f]	–
$r_{7,20}$	107.7(4)	107.9	93.0[f]	–
$a_{2,1,3}$	119.25(61)	118.56	116.4(3)	115.7[e]
$a_{2,1,4}$	119.27(32)	119.67	121.1(3)[d]	–
$a_{1,4,5}$	121.30(4)	121.28	121.0[f]	–
$a_{4,5,7}$	121.13(6)	121.09	121.1[f]	–
$a_{5,4,6}$	117.39(8)	117.44	117.1[f]	–
$a_{5,7,9}$	120.91(6)	120.92	121.5[f]	–
$a_{7,9,8}$	118.52(7)	118.54	117.9[f]	–
$a_{7,9,10}$	120.74(4)	120.73	120.3[f]	–
$a_{1,2,12}$	108.92(8)	108.93	109.4[f]	–
$a_{1,2,13}$	112.41(8)	112.42	109.4[f]	–
$a_{1,2,14}$	111.06(8)	111.07	109.4[f]	–
$a_{4,5,18}$	120.42(4)	120.42	119.4[f]	–
$a_{9,7,20}$	119.50(4)	119.50	119.2[f]	–
$\phi_{5,4,1,2}$	7.5[e]	8.49	7.7[f]	–
$\phi_{4,1,2,12}$	181.39[e]	181.39	182.2[f]	–
$\phi_{4,1,2,13}$	121.39[e]	121.39	122.3[f]	–
$\phi_{4,1,2,14}$	61.39[e]	61.39	62.3[f]	–

[a] All internuclear distances ($r_{i,j}$) are tabulated in picometers. [b] All angles ($a_{i,j,k}$) and dihedral angles ($\phi_{i,j,k,l}$) are tabulated in degrees. [c] Presented as an average of the XRD measurements of $r_{1,2}$ and $r_{1,3}$. [d] Presented as an average of the XRD measurements of $a_{2,1,4}$ and $a_{3,1,4}$. [e] No uncertainties available; not directly refined. [f] No uncertainties available; measured from *.cif* data.

The Nitrile Subunit. The nitrile subunit appears to be decoupled from the benzyl subunit; $r_{9,10}$, connecting the two, is the longest bonded distance of the π system in both the GED

{143.7(3) pm} and XRD {142.7(5) pm} solutions. In contrast to the XRD solution, in which a non-zero $a_{9,10,11}$ {117.5(4)°} is reported, no deviation from linearity is observed for the nitrile subunit in either the GED solution (if this parameter is included – it is removed for simplicity in the final model; see Supplementary Information) or in any of our theoretical calculations.

The C≡N bond, $r_{10,11}$, is the shortest internuclear distance between heavy nuclei in in both the GED {113.8(3) pm} and XRD {114.5(4) pm} solutions, and the only example of a bonded distance determined shorter in the former solution than the latter. We note that our theoretical calculations at the B2PLYP/CBS level considerably overestimate $r_{10,11}$, as is systematic for multiple bonds computed using theoretical methods that incorporate perturbation-theory-like correlation.[82] Common hybrid DFT functionals generally perform only fractionally better here; those used in this work determine $r_{10,11}$ to be 115.6(1) pm. We note that basis set completion affects $r_{10,11}$ more than any other internuclear distance; for the DFT functionals used in this work, the value of $r_{10,11}$ decreases by 1.25(3) pm on transition from cc-pVDZ to CBS-quality results, whereas all other internuclear distances decrease only by 0.84(3) pm over the same transition.

The Benzyl Subunit. Quinoidal distortion of the benzyl subunit (such that $r_{5,7} < r_{7,9} < r_{4,5}$) is observed for all theoretical results and both the GED and XRD solutions. This is characteristic of para-substituted benzyl subunits where one substituent is electron-withdrawing and the other electron-donating; it is straightforward to predict the quinoidal distortion *via* valence bond theory. All internuclear distances between heavy nuclei are well-determined by GED to within 0.9(1) pm and 2.0(5) pm of their B2PLYP/CBS and XRD values, respectively, and the ratio of $r_{4,5} : r_{5,7} : r_{7,9}$ is well-conserved between the B2PLYP/CBS theoretical calculations and GED and XRD solutions, suggesting that the geometry of the benzyl subunit is negligibly perturbed by intermolecular interaction.

The Dimethylamino Subunit. No discussion on the structure of DMABN is complete without comment on the inversion/pyramidalization angle (the terms are used interchangeably in the literature and, confusingly, often without clear definition) of the dimethylamino subunit. Here we use the most common definition of the inversion angle, ϑ, which we take to be the angle between the plane of the benzyl subunit and the plane containing N_1, C_2 and C_3; ϑ is dependent on $\phi_{5,4,1,2}$. Heine *et al.*[53] reported a non-negligible ϑ {10.8(2)°, 298 K; 11.9(3)°, 253 K} in their solid-state XRD structural solution; Kajimoto *et al.*[51] determined a larger vibrationally-averaged ϑ (15°) in the gas phase using microwave spectroscopy, but did not place an uncertainty on this value. The microwave spectroscopy of DMABN in the gas phase was recently revisited by Pratt *et al.*,[52] who determined a vibrationally-averaged ϑ {14.6°} that was somewhat smaller than Kajimoto *et al.*,[51] although a complete structural solution was not the object of their investigation and, to the best of our knowledge, was not reported. It has proved difficult to theoretically model ϑ at equilibrium; familiar DFT functionals including B3LYP and B3P86 yield near-C_{2v}-symmetric structures with $\vartheta \approx 0.0°$ when used with common basis sets belonging to the Pople/Dunning/Ahlrichs families, while post-Hartree-Fock Møller-Plesset perturbation theory and coupled-cluster CCSD/CCSD(T) methods, when used with the same basis sets, yield C_s-symmetric structures for which ϑ is thought to be overestimated. A compromise is found in the double-hybrid B2PLYP functional of Grimme, with which ϑ (14.3°) can be calculated in excellent agreement with that determined *via* microwave spectroscopy by Kajimoto *et al.*[51] (≈ 0.7° smaller) and Pratt *et al.*[52] (≈ 0.3° smaller), motivating our choice of this method for our highest-level theoretical calculations. We note that the difficulty associated with measuring ϑ at equilibrium in the gas phase is likely to be a consequence of the shallow double-minimum ($\phi_{5,4,1,2} = \pm 8.49°$; B2PLYP/CBS) profile (Figure 9) of the potential energy as a function of $\phi_{5,4,1,2}$

and the nearly non-existent barrier to inversion (< 0.1 kJ mol^{-1}, B2PLYP/CBS) through $\phi_{5,4,1,2}$ = 0.0°, the latter having been determined *via* optimization of this C_{2v}-symmetric first-order saddle point.

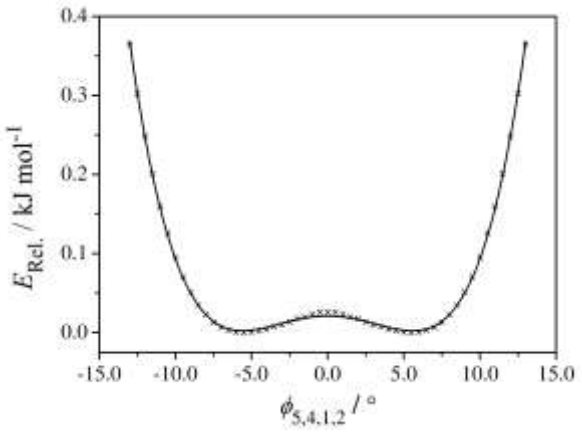

Figure 9. Potential energy of DMABN as a function of $\phi_{5,4,1,2}$, evaluated at the B2PLYP/CBS level. The continuous line represents a quartic function that has been fitted to the datapoints.

Inversion of the dimethylamino subunit can be expected to occur on a significantly shorter timescale (≈ 1 ps, estimated *via* vibrational frequency analysis) than that of the duration of our measurements using the electron beam in the University of York GED instrument; vibrational averaging consequently precluded our efforts to independently refine parameters p_{15} and p_{16} to give a measure of $\phi_{5,4,1,2}$, $\phi_{4,1,2,12}$, $\phi_{4,1,2,13}$ or $\phi_{4,1,2,14}$. *In lieu* of measurements for these parameters, a series of $R_G/R_{G,Min.}$ datapoints are presented in Figure 10, determined from twenty-six least-squares refinements in which $\phi_{5,4,1,2}$ was fixed at values between 0.0 and 13.0° (corresponding to a range of ϑ between 0.0 and ≈ 21.5°). Acknowledging the C_s symmetry of DMABN, a dual-minimum profile can be produced by reflection of the $R_G/R_{G,Min.}$ datapoints in the $\phi_{5,4,1,2}$ = 0.0° axis. A quartic function has been fitted to this dataset and the 95% confidence limit, representing approximately two standard deviations (2σ), has been indicated.

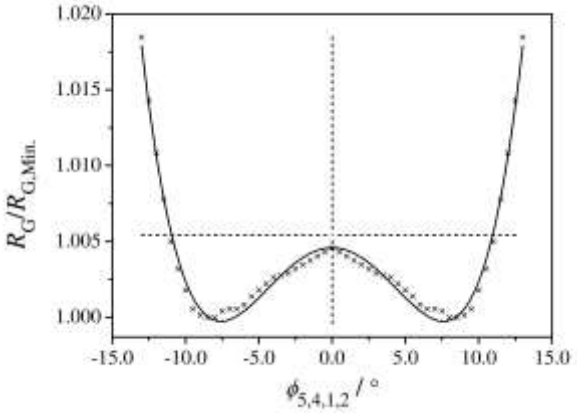

Figure 10. $R_G/R_{G,Min.}$, indicative of the quality of the least-squares refinement of DMABN, as a function of $\phi_{5,4,1,2}$. The continuous line represents a quartic function that has been fitted to the datapoints. The vertical dashed line represents $\phi_{5,4,1,2} = 0.0°$; the axis of reflection on account of the C_s symmetry of DMABN. The horizontal dashed line represents the 95% confidence limit, approximately equivalent to 2σ.

The minima in the quartic function represent the values of $\phi_{5,4,1,2}$ for which the best fit to the GED data is observed; these minima occur at $\phi_{5,4,1,2} = \pm 7.5°$, corresponding to an equilibrium ϑ of 12.7°. As predicted by our theoretical potential profile (Figure 9), which indicates that deviation from the theoretically-determined equilibrium $\phi_{5,4,1,2}$ is more favorable towards lower rather than higher angles, Figure 10 indicates that the quality of the least-squares refinement decreases less significantly when $\phi_{5,4,1,2}$ is set towards lower rather than higher angles. Indeed, we note that even at $\phi_{5,4,1,2} = 0.0°$, an acceptable refinement can be obtained with an $R_G/R_{G,Min.}$ beneath the 95% confidence limit; we are not able to determine unambiguously ϑ in favor of the C_s-symmetric pyramidalized structure and entirely rule out a hypothetical near-C_{2v}-symmetric equilibrium structure. Nonetheless, we note that our result for which the best fit to the GED data is observed is commensurate with ϑ being generally larger in the gas phase than in the solid state, as reported by Kajimoto *et al.*,[51] and is in good quantitative agreement with the revised gas-phase MWS result of Pratt *et al.*[52]

CONCLUSIONS.

The only gas electron diffractometer in the UK has been relocated to the University of York and recommissioned, reestablishing the UK among the group of less than half a dozen locations worldwide where gas electron diffraction experiments are carried out. The instrument has been fitted with an air-heated nozzle assembly to increase the range of samples accessible to study in the gas phase and has been introduced here alongside a description of the contemporary gas electron diffraction experiment. In a demonstration of the efficacy of the instrument for obtaining high-quality, gas-phase structures of isolated molecules, the structure of DMABN has been directly determined using the gas electron diffraction technique at high temperature in combination with complementary theoretical calculations. The agreement between experiment and theory, which is as good as 0.8(3) pm and 0.1(2)° for internuclear distances and angles, respectively, attests to the quality of our structural solution.

ASSOCIATED CONTENT.

Supporting Information. A summary of experimental parameters (Table S1), Cartesian coordinates and energies of DFT-optimized geometries (Tables S2-19), a description of the parameterized molecular model (Eq. S1-32), a summary of GED experimental parameters (Table S20), least-squares correlation matrix (Table S21), a summary of refined and theoretical refinable parameter values with SARACEN restraints (Table S22), a summary of fixed (non-refinable) parameter values (Table S23), r_a-type internuclear distances, refined and theoretic amplitudes of vibration and distance corrections with SARACEN restraints (Table S24), and the refined Cartesian coordinates for the GED-determined structure of DMABN (Table S25) may all

be accessed in the supporting information. This material is available free of charge via the Internet at http://pubs.acs.org

AUTHOR INFORMATION.

Corresponding Author

Derek A. Wann – contact *via* e-mail: derek.wann@york.ac.uk

Author Contributions

‡ These authors contributed equally.

All authors have given approval to the final version of the manuscript.

ACKNOWLEDGMENTS.

The research described in this article has been funded by the EPSRC, *via* a fellowship for DAW (EP/I004122) and a studentship for CDR (EP/1651146), by the University of York *via* the studentship of JPFN and by the Wild Fund Scholarship awarded to TLF. All data created during this research are available by request from the University of York Data Catalogue; see DOI: 10.15124/787c110d-2093-47c9-aefb-7e7d2f57c53a. We would like to thank the staff at the York Advanced Research Computing Cluster (YARCC) for allowing us access to their computational resources. We extend our thanks to the staff at the Mechanical Workshop and Electronics Workshop in the Department of Chemistry at University of York, especially Dr. Chris Rhodes (Electronics Workshop) and Stuart Murray (Mechanical Workshop), who have spent countless hours troubleshooting the GED instrument described in this article and modernizing much of the outdated technology. D.A.W would further like to thank Profs. David Rice and Elizabeth Page for useful discussions.

REFERENCES.

1. Zewail, A. H. Femtochemistry: Atomic-Scale Dynamics of the Chemical Bond. *J. Phys. Chem. A* **2000**, *104*, 5660–5694.

2. Zewail, A. H. 4D Ultrafast Electron Diffraction, Microscopy and Crystallography. *Ann. Rev. Phys. Chem.* **2006**, *57*, 65–103.

3. Sciaini, G.; Miller, R. J. D. Femtosecond Electron Diffraction: Heralding the Era of Atomically-Resolved Reaction Dynamics. *Rep. Prog. Phys.* **2011**, *74*, 096101.

4. Ischenko, A. A.; Weber, P. M.; Miller, R. J. D. Capturing Chemistry in Action with Electrons: Realization of Atomically-Resolved Reaction Dynamics. *Chem. Rev.* **2017**, *117*, 11066–11124.

5. Berger, R. J. F.; Hoffmann, M.; Hayes, S. A.; Mitzel, N. W. An Improved Gas Electron Diffractometer – The Instrument, Data Collection, Reduction and Structure Refinement Procedures. *Z. Naturforsch.* **2009**, *64*, 1259-1268.

6. Reuter, C. G.; Vishnevskiy, Y. V.; Blomeyer, S.; Mitzel, N. W. Gas Electron Diffraction of Increased Performance Through Optimization of Nozzle and System Design and Digital Control. *Z. Naturforsch.* **2016**, *71*, 1–13.

7. Girichev, G. V.; Utkin, A. N.; Revichev, Y. F. Modernization of GED Apparatus EMR-100 for Gas Investigation. *Prib. Tekh. Eksp.* **1984**, *2*, 187−190.

8. Girichev, G. V.; Shlykov, S. A.; Revichev, Y. F. Apparatus for Molecular Structure Investigations of the Valence-Unsaturated Compounds. *Prib. Tekh. Eksp.* **1986**, *4*, 167–169.

9. Hedberg, K. Fifty Years of Gas-Phase Electron Diffraction Structure Research: A Personal Retrospective. *Struct. Chem.* **2005**, *16*, 93–109.

10. Aarset, K.; Page, E. M.; Rice, D. A. Molecular Structures of 1,1-Dimethyl-1-silacyclopent-3-ene, $(CH_3)_2SiC_4H_6$, and 1,1-Dimethyl-1-germacyclopent-3-ene, $(CH_3)_2GeC_4H_6$, Obtained by Gas-Phase Electron Diffraction and Theoretical Calculations. *J. Phys. Chem. A* **1999**, *103*, 5574–5580.

11. Aarset, K.; Page, E. M. Molecular Structures of Trimethylchlorogermane, $(CH_3)_3GeCl$, and Trimethylbromogermane, $(CH_3)_3GeBr$, Obtained by Gas-Phase Electron Diffraction and Theoretical Calculations. *J. Phys. Chem. A* **2004**, *108*, 5474–5478.

12. Aarset, K.; Page, E. M.; Rice, D. A. Molecular Structure of 2,5-Dihydropyrrole (C_4NH_7), Obtained by Gas-Phase Electron Diffraction and Theoretical Calculations. *J. Phys. Chem. A* **2005**, *109*, 4961–4965.

13. Aarset, K.; Page, E. M.; Rice, D. A. Molecular Structures of Benzoic Acid and 2-Hydroxybenzoic Acid, Obtained by Gas-Phase Electron Diffraction and Theoretical Calculations. *J. Phys. Chem. A* **2006**, *110*, 9014–9019.

14. Aarset, K.; Page, E. M.; Rice, D. A. The Molecular Structure of Hexamethyldigermane Determined by Gas-Phase Electron Diffraction with Theoretical Calculations for $(CH_3)_3M{-}M(CH_3)_3$ Where M = C, Si, and Ge. *J. Phys. Chem. A* **2010**, *114*, 7187–7190.

15. Aarset, K.; Page, E. M.; Rice, D. A. Hydrogen Bonding in the Gas Phase: The Molecular Structures of 2-Hydroxybenzamide ($C_7H_7NO_2$) and 2-Methoxybenzamide ($C_8H_9NO_2$), Obtained by Gas-Phase Electron Diffraction and Theoretical Calculations. *J. Phys. Chem. A* **2013**, *117*, 3034–3040.

16. Johnsen, E.; Downs, A. J.; Greene, T. M.; Souter, P. F.; Aarset, K.; Page, E. M.; Rice, D. A.; Richardson, A. N.; Brain, P. T.; Rankin, D. W. H.; *et al.* Monochlorogallane: Physical Properties and Structure of the Gaseous Molecule $H_2Ga(\mu\text{-}Cl)_2GaH_2$ As Determined by Vibrational, Electron Diffraction, and Ab Initio Studies. *Inorg. Chem.* **2000**, *39*, 719–727.

17. Page, E. M.; Rice, D. A.; Hagen, K.; Hedberg, L.; Hedberg, K. Gas-Phase Electron-Diffraction Studies of the Molecular Structures of Tetrabromo(sulfido)tungsten(VI), $WSBr_4$, and Tetrabromo(seleno)tungsten(VI), $WSeBr_4$. *Inorg. Chem.* **1991**, *30*, 4758–4791.

18. Lippert, E.; Lüder, W.; Moll, F.; Nagele, W.; Boos, H.; Prigge, H.; Seybold-Blankenstein, I. Umwandlung von Elektronenanregungsenergie. *Angew. Chem.* **1961**, *73*, 695−706.

19. Grabowski, Z. R.; Rotkiewicz, K.; Grellmann, K. H. Reinterpretation of the Anomalous Fluorescense of *p*-N,N-Dimethylaminobenzonitrile. *Chem. Phys. Lett.* **1973**, *19*, 315−318.

20. Grabowski, Z. R.; Rotkiewicz, K.; Siemiarczuk, A.; Cowley, D. J.; Baumann, W. Twisted Intramolecular Charge Transfer States (TICT). A New Class of Excited States with Full Charge Separation. *Nouv. J. Chem.* **1979**, *3*, 443–446.

21. Kobayashi, T.; Futakami, M.; Kajimoto O. 4-(N,N-Dimethylamino)benzonitrile Solvated by a Polar Molecule: Structural Demand for Charge Transfer State Formation. *Chem. Phys. Lett.* **1986**, *130*, 63–66.

22. Kobayashi, T.; Futakami, M.; Kajimoto, O. The Charge Transfer State of 4-Dimethylamino-3,5-Dimethylbenzonitrile Studied in a Free Jet. *Chem. Phys. Lett.* **1987**, *141*, 450–454.

23. Zachariasse, K. A.; von der Haar, T.; Hebecker, A.; Leinhos, U.; Kühnle, W. Intramolecular Charge Transfer in Aminobenzonitriles: Requirements for Dual Fluorescence. *Pure Appl. Chem.* **1993**, *65*, 1745−1750.

24. Zachariasse, K. A.; Grobys, M.; Von der Haar, T.; Hebecker, A.; Il'ichev, Y. V.; Jiang, Y. B.; Morawski, O.; Kühnle, W. Intramolecular Charge Transfer in the Excited State: Kinetics and Configurational Changes. *J. Photochem. Photobiol. A* **1996**, *102*, 59–70.

25. Zachariasse, K. A.; Grobys, M.; Von der Haar, T.; Hebecker, A.; Il'ichev, Y. V.; Morawski, O.; Kühnle, W. Photo-Induced Intramolecular Charge Transfer and Internal Conversion in Molecules with a Small Energy Gap Between S_1 and S_2: Dynamics and Structure. *J. Photochem. Photobiol. A* **1997**, *105*, 373–383.

26. Zachariasse, K. A.; Druzhinin, S. I.; Kovalenko, S. A.; Senyushkina, T. Intramolecular Charge Transfer of 4-(N,N-Dimethylamino)benzonitrile Probed by Time-Resolved Fluorescence and Transient Absorption: No Evidence for Two ICT States and a πσ* Intermediate. *J. Chem. Phys. A* **2009**, *131*, 224313.

27. Sobolewski, A. L.; Domcke, W. Promotion of Intramolecular Charge Transfer in Dimethylamino Derivatives: Twisting Versus Acceptor-Group Rehybridization. *Chem. Phys. Lett.* **1996**, *259*, 119−127.

28. Sobolewski, A. L.; Sudholt, W.; Domcke, W. Ab Initio Investigation of Reaction Pathways for Intramolecular Charge Transfer in Dimethylanilino Derivatives. *J. Phys. Chem. A* **1998**, *102*, 2716−2722.

29. Perez Salgado, F.; Herbich, J.; Kunst, A. G. M.; Rettschnick, R. P. H. Structure and Picosecond Excited State Dynamics in Isolated, Supercooled 4-(N,N-Dimethylamino)benzonitrile. *J. Phys. Chem. A* **1999**, *103*, 3184−3192.

30. Parusel, A. B. J.; Köhler, G. A. Coupled-Cluster Analysis of the Electronic Excited States in Aminobenzonitriles. *J. Phys. Chem. A* **1999**, *103*, 4056− 4064.

31. Parusel, A. B. J.; Rettig, W.; Sudholt, W. A. Comparative Theoretical Study on DMABN: Significance of Excited State Optimized Geometries and Direct Comparison of Methodologies. *J. Phys. Chem. A* **2002**, *106*, 804−815.

32. Ma, C.; Kwok, W. M.; Matousek, P.; Parker, A. W.; Phillips, D.; Toner, W. T.; Towrie, M. Excited States of 4-Aminobenzonitrile (ABN) and 4-Dimethylaminobenzonitrile (DMABN): Time-Resolved Resonance Raman, Transient Absorption, Fluorescence, and Ab Initio Calculations. *J. Phys. Chem. A* **2002**, *106*, 3294−3305.

33. Sudholt, W.; Sobolewski, A. L.; Domcke, W. Ab Initio Study of the Amino Group Twisting and Wagging Reaction Paths in the Intramolecular Charger Transfer of 4-(N,N-Dimethylamino)benzonitrile. *Chem. Phys.* **1999**, *240*, 9−18.

34. Grabowski, Z. R.; Rotkiewicz, K.; Rettig, W. Structural Changes Accompanying Intramolecular Electron Transfer: A Focus on Twisted Intramolecular Charge Transfer States and Structures. *Chem. Rev.* **2003**, *103*, 3899−4032.

35. Trushin, S. A.; Yatsuhashi, T.; Fuß, W.; Schmid, W. E. Coherent Oscillations in the Charge Transfer System 4-(Dimethylamino)benzonitrile. *Chem. Phys. Lett.* **2003**, *376*, 282−291.

36. Rappoport, D.; Furche, F. Photoinduced intramolecular charge transfer in 4-(Dimethyl)aminobenzonitrile – A Theoretical Perspective. *J. Am. Chem. Soc.* **2004**, *126*, 1277−1284.

37. Köhn, A.; Hättig, C. On the Nature of the Low-Lying Singlet States of 4-(Dimethylamino)benzonitrile. *J. Am. Chem. Soc.* **2004**, *126*, 7399−7410.

38. Köhn, A.; Hättig, C.; Hellweg, A. Intramolecular Charge Transfer Mechanism in Quinolidines: The Role of the Amino Twist Angle. *J. Am. Chem. Soc.* **2006**, *128*, 15672−15682.

39. Gomez, I.; Reguero, M.; Boggio-Pasqua, M.; Robb, M. A. Intramolecular Charge Transfer in 4-Aminobenzonitriles Does Not Necessarily Need the Twist. *J. Am. Chem. Soc.* **2005**, *127*, 7119−7129.

40. Cogan, S.; Zilberg, S.; Haas, Y. The Electronic Origin of the Dual Fluorescence in Donor-Acceptor Substituted Benzene Derivatives. *J. Am. Chem. Soc.* **2006**, *128*, 3335−3345.

41. Fuß, W.; Schmid, W. E.; Pushpa, K. K.; Trushin, S. A.; Yatsuhashi, T. Ultrafast Relaxation and Coherent Oscillations in Aminobenzonitriles in the Gas Phase Probed by Intense Field Ionization. *Phys. Chem. Chem. Phys.* **2007**, *9*, 1151−1169.

42. Lee, J.-K.; Fujiwara, T.; Kofron, W. G.; Zgierski, M. Z.; Lim, E. C. The Low-Lying πσ* State and its Role in the Intramolecular Charge Transfer of Aminobenzonitriles and Aminobenzethyne. *J. Chem. Phys.* **2008**, *128*, 164512.

43. Zgierski, M. Z.; Fujiwara, T.; Lim, E. C. Conical Intersections and Ultrafast Intramolecular Excited State Dynamics in Nucleic Acid Bases and Electron Donor-Acceptor Molecules. *Chem. Phys. Lett.* **2008**, *463*, 289−299.

44. Coto, P. B.; Gustavsson, T.; Serrano-Andres, L.; Fujiwara, T.; Lim, E. C. Do Fluorescence and Transient Absorption Probe the Same Intramolecular Charger Transfer State of 4-(Dimethylamino)benzonitrile? *J. Chem. Phys.* **2009**, *131*, 031101.

45. Coto, P. B.; Serrano-Andres, L.; Gustavsson, T.; Fujiwara, T.; Lim, E. C. Intramolecular Charge Transfer and Dual Fluorescence of 4-(Dimethylamino)benzonitrile: Ultrafast Branching Followed by a Two-Fold Decay Mechanism. *Phys. Chem. Chem. Phys.* **2011**, *13*, 15182–15188.

46. Park, M.; Kim, C. H.; Joo, T. Multifaceted Ultrafast Intramolecular Charge Transfer Dynamics of 4-(Dimethylamino)benzonitrile (DMABN). *J. Phys. Chem. A* **2013**, *117*, 370–377.

47. Georgieva, I.; Aquino, A. J. A.; Plasser, F.; Trendafilova, N.; Köhn, A.; Lischka, H. Intramolecular Charge Transfer Excited-State Processes in 4-(N,N-Dimethylamino)benzonitrile: The Role of Twisting and the πσ* State. *J. Phys. Chem. A* **2015**, *119*, 6232–6243.

48. Kochman, M. A.; Tajti, A.; Morrison, C. A.; Miller, R. J. D. Early Events in the Nonadiabatic Relaxation Dynamics of 4-(N,N-Dimethylamino)benzonitrile. *J. Chem. Theory Comput.* **2015**, *11*, 1118–1128.

49. Du, L.; Lan, Z. An On-The-Fly Surface-Hopping Program JADE for Nonadiabatic Molecular Dynamics of Polyatomic Systems: Implementation and Applications. *J. Chem. Theory Comput.* **2015**, *11*, 1360−1374.

50. Curchod, B. F. E.; Sisto, A.; Martínez, T. J. Ab Initio Multiple Spawning Photochemical Dynamics of DMABN Using GPUs. *J. Phys. Chem. A* **2017**, *121*, 265–276.

51. Kajimoto, O.; Yokoyama, H.; Ooshima, Y.; Endo, Y. The Structure of 4-(N,N-Dimethylamino)benzonitrile and its Van der Waals Complexes. *Chem. Phys. Lett.* **1991**, *179*, 455–459.

52. Bird, R. G.; Neill, J. L.; Alstadt, V. J.; Young, J. W.; Pate, B. H.; Pratt. D. W. Ground State ^{14}N Quadrupole Couplings in the Microwave Spectra of N,N-Dimethylaniline and 4,4-Dimethylminobenzonitrile. *J. Phys. Chem. A* **2011**, *115*, 9392–9398.

53. Heine, A.; Herbst-Irmer, R.; Stalke, D.; Kühnle, W.; Zachariasse, K. A. Structure and Crystal Packing of 4-Aminobenzonitriles and 4-Amino-3,5-Dimethylaminobenzonitriles at Various Temperatures. *Acta Crystallogr. B* **1994**, *50*, 363–373.

54. Mitzel, N. W.; Brown, D. H.; Parsons, S.; Brain, P. T.; Pulham, C. R.; Rankin, D. W. H. Differences Between Gas-Phase and Solid-State Molecular Structures of the Simplest Phosphonium Ylide, $Me_3P{=}CH_2$. *Angew. Chem. Int. Ed.* **1998**, *37*, 1670–1672.

55. Mitzel, N. W.; Lustig, C.; Berger, R. J. F.; Runeberg, N. Luminescence Phenomena and Solid-State Structures of Trimethyl and Triethylgallium. *Angew. Chem. Int. Ed.* **2002**, *41*, 2519–2522.

56. Mitzel, N. W.; Vojinovic, K.; Foerster, T.; Robertson, H. E.; Borisenko, K. B.; Rankin, D. W. H. (Dimethylaminomethyl)trifluorosilane, $Me_2NCH_2SiF_3$—A Model for the α-Effect in Aminomethylsilanes. *Chem. Eur. J.* **2005**, *11*, 5114–5125.

57. Hagemann, M.; Mix, A.; Berger, R, J. F.; Pape, T.; Mitzel, N. W. Strong Intramolecular Si−N Interactions in the Chlorosilanes $Cl_{3-n}H_nSiOCH_2CH_2NMe_2$ (n = 1−3) *Inorg. Chem.* **2008**, *47*, 10554–10564.

58. Hagemann, M.; Berger, R. J. F.; Hayes, S. A.; Stammler, H. G.; Mitzel, N. W. N,N-Dimethylaminopropylsilane: A Case Study on the Nature of Weak Intramolecular Si···N Interactions. *Chem. Eur. J.* **2008**, *14*, 11027–11038.

59. Bonham, R. A.; Fink, M. *High Energy Electron Scattering*; Van Nostrand Reinhold Co.: New York, United States of America, 1974.

60. Frisch, M. J.; Trucks, G. W.; Schlegel, H. B.; Scuseria, G. E.; Robb, M. A.; Cheeseman, J. R.; Scalmani, G.; Barone, V.; Mennucci, B.; Petersson, G. A.; *et al.* Gaussian 09, Revision D.01; Gaussian, Inc.: Wallingford CT, 2009.

61. Grimme, S. Semiempirical Hybrid Density Functional with Perturbative Second-Order Correlation. *J. Chem. Phys.* **2006**, *124*, 034108.

62. Dunning, T. H., Jr. Gaussian Basis Sets for Use in Correlated Molecular Calculations. I. The Atoms Boron Through Neon and Hydrogen. *J. Chem. Phys.* **1989**, *90*, 1007–1023.

63. Mitzel, N. W.; Smart, B. A.; Blake, A. J.; Robertson, H. E.; Rankin, D. W. H. Conformational Analysis of 1,4-Disilabutane and 1,5-Disilapentane by Combined Application of Gas-Phase Electron Diffraction and *Ab Initio* Calculations and the Crystal Structure of 1,5-Disilapentane at Low Temperatures. *J. Phys. Chem. A* **1996**, *100*, 9339–9347.

64. Blake, A. J.; Brain, P. T.; McNab, H.; Miller, J.; Morrison; C. A.; Parsons, S.; Rankin, D. W. H.; Robertson, H. E.; Smart, B. A. Structure Analysis Restrained by *Ab Initio* Calculations: The Molecular Structure of 2,5-Dichloropyrimidine in Gaseous and Crystalline Phases. *J. Phys. Chem. A* **1996**, *100*, 12280–12287.

65. Mitzel, N. W.; Rankin, D. W. H. SARACEN – Molecular Structures from Theory and Experiment: The Best of Both Worlds. *Dalton Trans.* **2003**, 3650–3662.

66. Becke, A. D. Density-Functional Thermochemistry. III. The Role of Exact Exchange. *J. Chem. Phys.* **1993**, *98*, 5648-5652.

67. Lee, C.; Yang, W.; Parr., R. G. Development of the Colle-Salvetti Correlation Energy Formula into a Functional of the Electron Density. *Phys. Rev. B* **1988**, *37*, 785–789.

68. Perdew, J. P. Density-Functional Approximation for the Correlation Energy of the Inhomogeneous Electron Gas. *Phys. Rev. B* **1986**, *33*, 8822–8824.

69. Perdew, J. P.; Chevary, J. A.; Vosko, S. H.; Jackson, K. A.; Pederson, M. R.; Singh, D. J.; Fiolhais, C. Atoms, Molecules Solids and Surfaces - Applications of the Generalized Gradient Approximation for Exchange and Correlation. *Phys. Rev. B* **1992**, *46*, 6671–6687.

70. Ernzerhof, M.; Perdew, J. P. Generalized Gradient Approximation to the Angle and System Averaged Exchange Hole. *J. Chem. Phys.* **1998**, *109*, 3313–3320.

71. Heyd, J.; Scuseria, G. Efficient Hybrid Density Functional Calculations in Solids: The HS-Ernzerhof Screened Coulomb Hybrid Functional. *J. Chem. Phys.* **2004**, *121*, 1187-1192.

72. Heyd, J.; Scuseria, G. Assessment and Validation of a Screened Coulomb Hybrid Density Functional. *J. Chem. Phys.* **2004**, *120*, 7274-7280.

73. Heyd, J.; Peralta, J. E.; Scuseria, G.; Martin, R. L. Energy Band Gaps and Lattice Parameters Evaluated with the Heyd-Scuseria-Ernzerhof Screen Hybrid Functional. *J. Chem. Phys.* **2005**, *123*, 174101.

74. Heyd, J.; Scuseria, G.; Ernzerhof, M. Erratum: Hybrid Functionals Based on a Screened Coulomb Potential. *J. Chem. Phys.* **2006**, *124*, 219906.

75. Sipachev, V. A. Calculation of Shrinkage Corrections in the Harmonic Approximation. *J. Mol. Struct. THEOCHEM* **1985**, *22*, 143-151.

76. Sipachev, V. A. Local Centrifugal Distortions Caused by Internal Motions of Molecules. *J. Mol. Struct.* **2001**, *567*, 67–72.

77. Nunes, J. P. F. University of York, Heslington, United Kingdom. Personal Communication, 2017.

78. Hinchley, S. L.; Robertson, H. E.; Borisenko, K. R.; Turner, A. R.; Johnston, B. F.; Rankin, D. W. H.; Ahmadian, M.; Jones, J. N.; Cowley, A. H. The Molecular Structure of Tetra-*tert*-butyldiphosphine: An Extremely Distorted, Sterically Crowded Molecule. *Dalton Trans.* **2004**, 2469–2476.

79. Ross, A. W.; Fink, M.; Hilderbrandt, R. *International Tables for Crystallography*; Wilson, A. J. C., Ed.; Kluwer Academic Publishers: Dordrecht, Netherlands, 1992, Vol. C.

80. Masters, S. L.; Atkinson, S. J.; Hölbling, M.; Hassler, K. Gas-Phase Molecular Structure of 1,1,1,2-tetrabromo-2,2-dimethyldisilane: Theoretical and Experimental Investigation of a Super-Halogenated Disilane and Computational Investigation of the F, Cl and I Analogues. *Struct. Chem.* **2013**, *24*, 1201–1206.

81. Rankin, D. W. H. *Stereochemical Applications of Gas-Phase Electron Diffraction*; Hargittai, I.; Hargittai, M, Ed.; VCH Publishers Inc.: New York, United States of America, 1988.

82. Hehre, W. J.; Radom, L.; Schleyer, P. v. R.; Pople, J. A. *Ab Initio Molecular Orbital Theory*; Wiley: New York, United States of America, 1986.

TOC GRAPHIC.